Nonlinear Optical Materials | Hot Paper

Prediction of Novel van der Waals Boron Oxides with Superior Deep-Ultraviolet Nonlinear Optical Performance

Hao Li[+], Jingmei Min[+], Zhihua Yang,* Zhenhai Wang,* Shilie Pan,* and Artem R. Oganov*

Abstract: *Deep-ultraviolet nonlinear optical (DUV NLO) materials are attracting increasing attention because of their structural diversity and complexity. Using the two-dimensional (2D) crystal structure prediction method combined with the first-principles calculations, here we propose layered 18-membered-ring (18MR) boron oxide B_2O_3 polymorphs as high-performance NLO materials. 18MR-B_2O_3 with the AA and AB stackings are potential DUV NLO materials. The superior performing 18MR-$B_2O_3^{AB}$ has an unprecedentedly high second harmonic generation coefficient of 1.63 pmV⁻¹, the largest among the DUV NLO materials, three times larger than that of the advanced DUV NLO material $KBe_2BO_3F_2$ and comparable to that of β-BaB_2O_4. Its unusually large birefringence of 0.196 at 400 nm guarantees the phase-matching wavelength λ_{PM} to reach this material's extreme absorption edge of ≈ 154 nm.*

Introduction

Crystal structure prediction based on the density functional theory (DFT) has been used to accelerate the advanced materials discovery,[1] with plenty of successful cases reported.[2] Particularly, deep-ultraviolet ($\lambda \leq 200$ nm) nonlinear optical (DUV NLO) materials,[3] which can expand the DUV frequency range via a frequency conversion by all-solid-state lasers, are increasingly required for numerous

applications in laser spectroscopy, laser microprocessing, laser surgery, and optical communications.[4] However, strict property criteria are required for such materials,[5] including a wide transparency window in the DUV region, which is equivalent to a large band gap (≥ 6.20 eV); sufficient birefringence to ensure the phase-matching (PM) wavelength λ_{PM} in the DUV region; and large second harmonic generation (SHG) coefficient ($\geq 1 \times d_{36}(KH_2PO_4, KDP) = 0.39$ pmV⁻¹).

Borates have attracted sustained attention in structure prediction,[6] design,[7] and synthesis[8] as promising UV NLO candidates.[9] The introduction of fluorine, having a large electronegativity, for shifting the cutoff edge and λ_{PM} to the DUV region is a preferred strategy.[10] So far, the $KBe_2BO_3F_2$ (KBBF)[11] and $NH_4B_4O_6F$ (ABF)[12] families of promising DUV NLO materials with excellent properties have been obtained in experiment. In these compounds, the fluorine atom plays a main regulatory role for the cutoff edge and optical properties. However, besides the introduction of fluorine, can other design approaches be used in order to meet the strict criteria?

For borates, according to the anionic group theory,[13] the [BO$_x$] units with the B-O covalent bonds are the dominating active units for the NLO properties. In general, metal cations, mainly alkali and alkaline-earth cations, contribute negligibly to the overall NLO coefficients. Plain π-conjugated [BO$_3$] is recognized as one of the best UV/DUV NLO active units, whereas dangling bonds are not beneficial to the DUV transmittance. To eliminate the dangling bonds, researchers introduce substitutions to reduce the density of terminal oxygens getting [BeO$_3$F] or [BO$_3$F] in KBBF and ABF, respectively. To realize a strong NLO response, the arrangement of the units is also critical. Novel NLO materials with highly polymerized [BO$_3$] units in optimal arrangements are eagerly anticipated.

In this work, we propose a novel prediction process based on the features of layered van der Waals (vdW) materials and use it to successfully predict a vdW material B_2O_3. In such materials, layers connected by the vdW forces and no metal cations are required, which is widely applied in many fields.[14] Different from the commonly used prediction of vdW materials,[15] the approach that we propose consists of two steps. First, 2D B_2O_3 layers are predicted to maintain the effective SHG motif [BO$_3$]. The dangling bond on the O atoms can be self-eliminated because the intralayer [BO$_3$] units are connected by corner-shared O atoms. Second, we stack the 2D layers in diverse ways to obtain 3D bulk B_2O_3, a process that resembles turning graphene into graphite. The parallel 2D layer stackings are preferred for the NLO properties of bulk B_2O_3. Consequently, three kinds of B_2O_3 layers are obtained, among them the 18-membered-ring

[*] H. Li,[+] J. Min,[+] Prof. Z. Yang, Prof. S. Pan
CAS key Laboratory of Functional Materials and Devices for Special Environments; Xinjiang Technical Institute of Physics & Chemistry, CAS; Xinjiang Key Laboratory of Electronic Information Materials and Devices
40-1 South Beijing Road, Urumqi 830011 (China)
E-mail: zhyang@ms.xjb.ac.cn
slpan@ms.xjb.ac.cn

H. Li,[+] Prof. Z. Yang, Prof. S. Pan
Center of Materials Science and Optoelectronics Engineering, University of Chinese Academy of Sciences
Beijing 100049 (China)

H. Li,[+] Z. Wang, Prof. A. R. Oganov
Skolkovo Institute of Science and Technology, Skolkovo Innovation Center, 3 Nobel St., Moscow 121025 (Russia)
E-mail: a.oganov@skoltech.ru

Z. Wang
School of Telecommunication and Information Engineering, Nanjing University of Posts and Telecommunications
Nanjing, Jiangsu 210003 (China)
E-mail: wangzh@njupt.edu.cn

[+] These authors contributed equally to this work.

Supporting information and the ORCID identification number(s) for the author(s) of this article can be found under https://doi.org/10.1002/anie.202015622.

(18MR) B_2O_3 layer with a 1:1 ratio of [BO_3] and [B_3O_6] is considered to have the highest probability to exist and deserves further study. Five stacking arrangements were tried construct the 18MR-B_2O_3 bulk. Among them, the *AA* and *AB* stackings crystallize in noncentrosymmetric space groups. Finally, the two layered bulks that can meet the stringent requirements for DUV materials are investigated. In particular, the *AB* stacking of 18MR-B_2O_3 exhibits a large band gap of 8.08 eV, which means a wide DUV transmission range, and a strong SHG effect that is 3 times that of KBBF and comparable to that of β-BaB_2O_4, thus showing a balance between the large band gap and SHG effect. Moreover, this material's large birefringence of 0.196 guarantees an extremely short phase-matching wavelength of 154 nm.

Results and Discussion

Structure description

The predicted low-energy structures of 2D B_2O_3 (Figure 1) display 12MR, 18MR, and 24MR topologies, in which the ring edges correspond to the [BO_3] triangles, alternating [BO_3] triangles and [B_3O_6] boroxol rings, and [B_3O_6] boroxol rings, respectively. The stability of these structures is verified by phonon calculations (Supporting Information Figure S1). The structural energy E decreases systematically as the number of the ring members increases: E (12MR-B_2O_3, −8.012 eV/atom) > E (18MR-B_2O_3, −8.032 eV/atom) > E (24MR-B_2O_3, −8.037 eV/atom). The structures of 12MR- and 24MR-B_2O_3 are constructed by placing either [BO_3] or [B_3O_6] in the node positions based on the topology of graphene.[16] Graphene belongs to centrosymmetric space group $P6/mmm$, whereas the symmetry of 12MR- and 24MR-B_2O_3 is reduced to noncentrosymmetric subgroup P-62 m because the introduction of [BO_3] or [B_3O_6] without a two-fold rotation axis breaks the inversion symmetry of the parent group. A similar process occurs when [BO_3] and [B_3O_6] are placed alternately in the graphene nodes around the ring: 18MR-B_2O_3 lacks a mirror operation and has a lower $P\bar{6}$ symmetry. Only one crystallographically equivalent boron exists in 12MR-B_2O_3 and 24MR-B_2O_3, whereas 18MR-B_2O_3 has two crystallo-
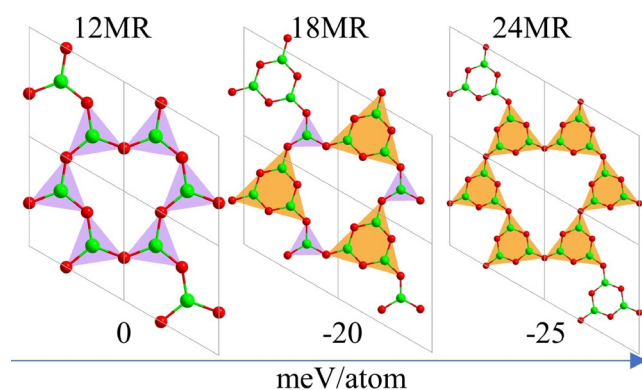
Figure 1. Structures of 12MR-B_2O_3, 18MR-B_2O_3, and 24MR-B_2O_3 with their energies per atom. The energy of 12MR-B_2O_3 (−8.012 eV/atom) is set as a reference.
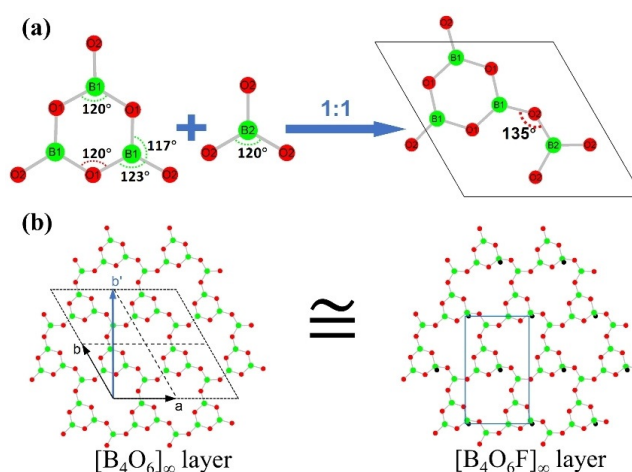
Figure 2. a) 18MR-B_2O_3 consists of [BO_3] and [B_3O_6] (1:1). b) The layer regarded as [B_4O_6]$_\infty$ is highly similar to [B_4O_6F]$_\infty$ in ABF.
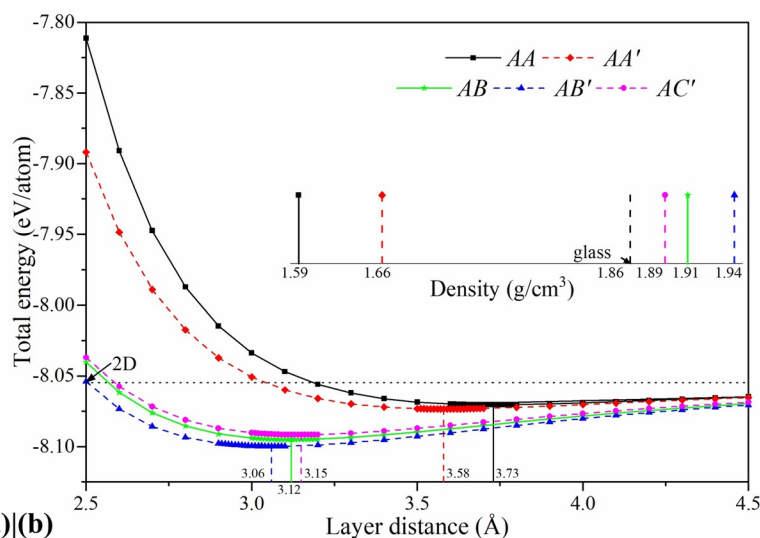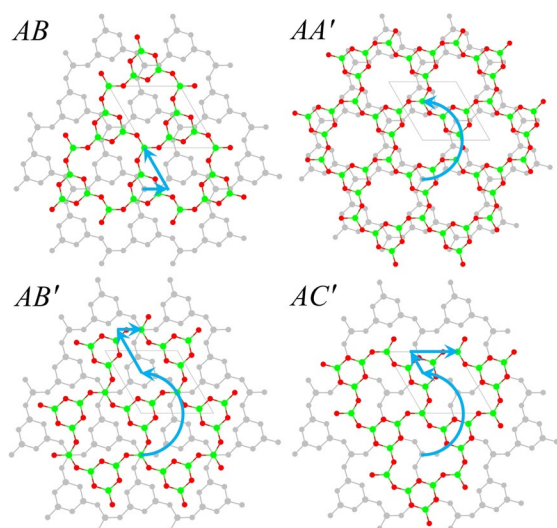
graphically different boron positions (Figure 2) because of its lower symmetry.

Feasibility of 18MR-B_2O_3

The three predicted 2D layers are novel and have not been found among the known crystalline B_2O_3 polymorphs (B_2O_3-I and B_2O_3-II),[17] which have 3D frameworks consisting of the [BO_3] and [BO_4] units, respectively. Layered structures are common in metal-containing borates, and they increase the confidence in the existence of the predicted 2D layers of B_2O_3. In the KBBF[11a,b] family, each [BO_3] group links up with a metal cationic polyhedron, including [BeO_4], [AlO_4], [AlO_3F], and [ZnO_3F_2], forming the 12MR layers of [$Be_3B_3O_6$]$_\infty$,[11b,18] [$Al_3B_3O_6$]$_\infty$,[19] [$Al_3(BO_3)_3OF$]$_\infty$,[20] and [$ZnBO_3F$]$_\infty$,[21] respectively. At the same time, 12MR and 24MR formations composed of only the [BO] group have not been found in metal-containing borates. 18MR-B_2O_3 is expected to be the optimal structure on the basis of the following considerations. (i) **Composition.** 18MR-B_2O_3 is formed by boroxol [B_3O_6] and independent [BO_3] group (1:1). The previous NMR measurements of vitreous (glassy) boron trioxide (v-B_2O_3)[22] show approximately the same 1:1 ratio of these units, providing the material base for further experimental synthesis of 18MR-B_2O_3. (ii) **Structure.** The counterpart of 18MR-B_2O_3 has been uncovered among the known compounds. In 18MR-B_2O_3, the [BO_3] and [B_3O_6] groups connect with each other to form the [B_4O_6]$_\infty$ layer with the structure similar to the 2D wavelike [B_4O_6F]$_\infty$ layer in fluorooxoborate ABF and its family. 18MR-B_2O_3 has hexagonal symmetry (Figure 2), but its corresponding orthorhombic cell has the parameters $a = 6.700$ Å and $b = 11.605$ Å. The [B_4O_6F]$_\infty$ layer, paving the bc plane of ABF, has the lattice parameters $b = 6.5952$ Å and $c = 11.197$ Å. Larger lattice parameters of 18MR-B_2O_3 than those of the [B_4O_6F]$_\infty$ layer are due to the entirely flat geometry of the [B_4O_6]$_\infty$ layer. The most revealing evidence is that exactly the same layer has been found in the $A_3HB_4S_2O_{14}$ (A = Rb, Cs)

10792 www.angewandte.org

© 2021 Wiley-VCH GmbH

Angew. Chem. Int. Ed. **2021**, 60, 10791–10797

crystals.[23] (iii) **Energy.** Although the energy of 18MR-B_2O_3 is higher than that of 24MR-B_2O_3 by 5 meV/atom in the 2D layer, the results for the 3D bulk are worth exploring. Layered bulk B_2O_3 can be further constructed using different stackings of three predicted 2D layers. For 18MR-B_2O_3, bulks with five stackings were constructed: AA, AB, AA', AB', and AC' (Figure 3 a). The AA stacking keeps identical in-plane positions, whereas the other four stackings are obtained by symmetrically transforming the original layer A. In the AB stacking, the second layer B is the result of a translation of the first layer A by (1/3, 2/3) along the a and b axes. The bilayer in ABF inspired the AA' stacking, in which the A' layer is produced by a 180° rotation of layer A around the center of the ring, resulting in the bilayer with an inversion center. In the AB' and AC' stackings, the B' and C' layers are generated via a translation of layer A' by (1/3, 2/3) and (2/3, 1/3), respectively. 18MR-$B_2O_3^{AB'}$ is exactly the previously predicted B_2O_3 polymorph.[24]
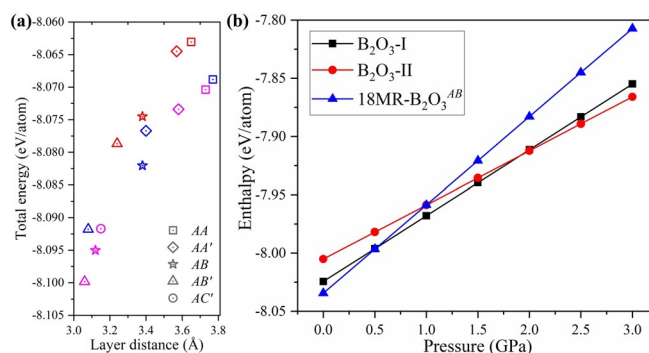
The dependence of the total energy with vdW corrected on the layer distance for these five stackings is shown in Figure 3 b. When the layers are far apart, the total energy of each stacking equals the energy of a 2D layer. As the layer spacing decreases, the total energy slowly becomes smaller. As the interlayer spacing decreases below equilibrium interlayer distance (EID), the total energy starts to increase sharply because of the growing repulsion due to overlap of electronic orbitals of the layers. The AA and AA' stackings have the EIDs of 3.73 and 3.58 Å, respectively. The EIDs of the AB, AB', and AC' stackings are shorter at 3.12, 3.06, and 3.15 Å, respectively. The difference in the EID is due to the interlayer geometry: in the AB, AB', and AC' stackings, the ring channels are occupied by the $[BO_3]$ or $[B_3O_6]$ units, making the repulsion forces weaker than those in the AA and AA' stackings, which results in shorter EIDs. As a consequence, the AB, AB', and AC' stackings are more stable energetically than the AA and AA' stackings.

The bulk density of stackings at the EID is shown in the inset in Figure 3 b. The density of the equilibrated AB, AB', and AC' stackings is very close to the experimental value of 1.84 g cm^{-3} for the v-B_2O_3 glass.

Similar to 18MR-B_2O_3, four 24MR-B_2O_3 stackings—AA, AB, AA', and AB'—were constructed. Their energies with vdW corrected are shown in Figure 4 a. Although the energy of a single two-dimensional 18MR-B_2O_3 layer is higher by 5 meV/atom than that of a single layer of 24MR-B_2O_3 18MR-B_2O_3 bulks exhibit lower energy. For the lowest-energy AB' stacking, 18MR-$B_2O_3^{AB'}$ has an advantage of 17.7 meV/atom over 24MR-$B_2O_3^{AB'}$. The comparison without accounting vdW energies of 18MR-$B_2O_3^{AB}$ with the known crystalline B_2O_3-I and B_2O_3-II shows that B_2O_3-I is more stable than B_2O_3-II at pressures below 2.0 GPa, whereas 18MR-$B_2O_3^{AB}$ is more stable than B_2O_3-I below 0.5 GPa. (Figure 4 b, Please see more details about the influence of vdW correction on energy differences in Supporting Information Figure S2) These properties make it interesting to synthesize 18MR-B_2O_3.

Figure 4. a) Total energy with vdW corrected of 12MR-B_2O_3 (red), 18MR-B_2O_3 (pink) and 24MR-B_2O_3 (blue) with the equilibrium interlayer distance. b) Pressure dependence of the enthalpy without vdW energy.

Figure 3. a) Formation of various 18MR-B_2O_3 stackings: the new layers B, A', B', and C' are obtained using different rotation or translation operations, or both, on the original layer A (gray). b) Total energy with vdW corrected vs. layer distance for different 18MR-B_2O_3 stackings compared with the total energy of a 2D layer. The bulk density of stackings at the equilibrium interlayer distance and of the B_2O_3 glass is shown in the inset.

Experimental suggestions

The analysis above suggests a high probability of existence of 18MR-B_2O_3, making its experimental synthesis very desirable for further studies. Here we suggest two experimentally feasible methods. (i) Choosing suitable seeds or substrates to grow the 18MR-B_2O_3 layers, including the [BOF] surface of the ABF family, (001) surface of the $A_3HB_4S_2O_{14}$ (A = Rb, Cs) crystals, and other (111) surfaces of face-centered cubic metals with the appropriate unit cell parameters. (ii) Thermal decomposition of ABF ($NH_4B_4O_6F \rightarrow NH_3\uparrow + HF\uparrow + 2B_2O_3$), decomposing the ABF crystals at around 300 °C to degas the interlayer ions F^- and NH_4^+ and obtaining a layered bulk of 18MR-B_2O_3.

NLO properties

Crystallization in a noncentrosymmetric space group is a necessary condition for compounds to produce the second-order NLO effects. Only the *AA* and *AB* stackings belong to a noncentrosymmetric space group $P\bar{6}$. According to the Kleinman symmetry, the $\bar{6}$ point group has two independent SHG coefficients, d_{11} and d_{22}. The calculated NLO-related properties of the *AA* and *AB* stackings and the most typical NLO crystals KBBF, ABF, and β-BaB_2O_4 (BBO)[25] are listed in Table 1. The maximum values of the SHG coefficients are $d_{11} = 1.46$ and 1.63 pm V^{-1} for the *AA* and *AB* stackings, respectively. The SHG responses of the *AA* and *AB* stackings are 3.1 and 3.4 times higher than that of KBBF and 1.2 and 1.4 times higher than that of ABF. They are comparable to the maximum SHG response of BBO ($d_{22} = 1.93$ pm V^{-1}, calculated). The extremely large SHG coefficients in the *AA* and *AB* stackings reflect high efficiency of frequency conversion, which is vital for the DUV region. Furthermore, their band gaps both reach the DUV region, especially that of the *AB* stacking at 8.08 eV (HSE06), which means its ability to make the DUV 154 nm wavelength transmission. Remarkably, the birefringence values at 400 nm of the *AA* and *AB* stackings are large, 0.186 and 0.196, respectively. To the best of our knowledge, the *AB* stacking has the highest birefringence among the DUV materials, including α-BBO,[26] Ca(BO_2)$_2$,[27] and MgF$_2$.[28] Large birefringences are favorable to PM for both stackings, and λ_{PM} for the type I PM process reaches their corresponding cutoff edges of 166 and 154 nm, a conclusion based on the calculated refractive dispersion curves (Supporting Information Figure S3). The *AB* stacking shows a shorter

PM wavelength than that of KBBF (161 nm) and ABF (158 nm). These results indicate that both stackings give promising as DUV NLO crystals.

Electronic structure

Exploration of electronic structures is pivotal for finding the relationship between the material structure and optical properties. The electronic band structures of the *AA* and *AB* stackings calculated using the Perdew-Burke-Ernzerhof (PBE) functional are shown in Figure 5. The *AB* stacking
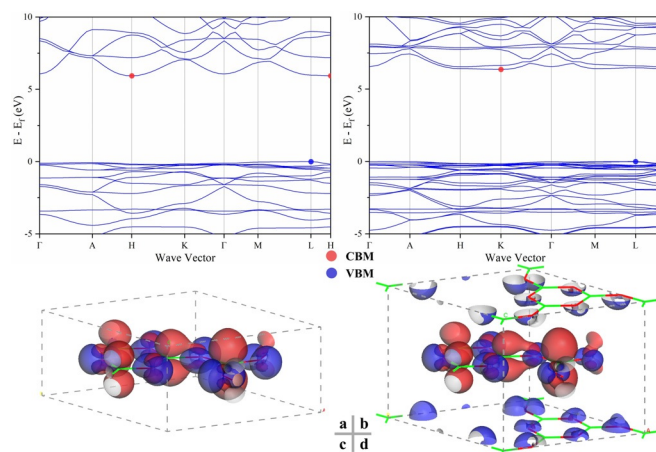
Figure 5. a, b) Band structure and c, d) valence band maximum (VBM) and conduction band minimum (CBM) of the *AA* and *AB* stackings.

has a wider band gap of 6.36 eV, whereas for the *AA* stacking, the band gap calculated using the PBE-GGA approach is 5.94 eV. They are both indirect gap compounds, with the valence band maximums (VBM) located at the L point, whereas their conduction band minimums (CBM) are located at the H and K points, respectively. The VBM and CBM orbitals of the *AA* and *AB* stackings are shown in Figures 5 c,d. VBM states at L are derived from the nonbonding 2p states of the O atoms. The CBM states are derived from the (π, π*) states of layers in both stackings (Figure 5 d), where the π bond orbital in the CBM stems from the in-ring B atoms and out-ring O atoms in boroxol. Therefore, both band gaps are determined by the nonbonding 2p states of the O atoms in the VBM and the (π, π*) states in the CBM.

Table 1: Calculated band gap, birefringence, and d_{ij} of the *AA* and *AB* stackings compared with the experimental values for ABF, KBBF, and BBO.

Structure	Space group	Bandgap [eV]	Birefringence at 400 nm	NLO coefficient d_{ij} [pm V^{-1}]	Cutoff Edge [nm]	Shortest λ_P [nm]
18MR-$B_2O_3^{AA[a]}$	$P\bar{6}$	7.49	0.186	$d_{11} = -0.98$; $d_{22} = 1.46$	166	166
18MR-$B_2O_3^{AB[a]}$	$P\bar{6}$	8.08	0.196	$d_{11} = -1.09$; $d_{22} = 1.63$	154	154
ABF[b]	$Pna2_1$	7.95	0.131	$d_{31} = 0.02$; $d_{32} = 1.07$; $d_{33} = -1.19$	156	158
KBBF[c]	$R32$	8.44	0.088	$d_{11} = 0.47(\pm 0.01)$	147	161
BBO[a]	$R3c$	6.45	0.111	$d_{22} = 1.93$; $d_{31} = -0.10$; $d_{33} = -0.02$	193	212
BBO[d]	$R3c$	6.56	0.1	$d_{22} = \pm 2.3$; $d_{31} = \mp 0.16$; $d_{33} \approx 0.00$	189	205

[a] This work; [b] ref. [12a]; [c] ref. [11a]; [d] ref. [25b].

Mechanism of NLO properties

Band-resolved calculations are utilized to investigate the respective contribution of each electron state to the SHG coefficients, whereas the partial density of states (PDOS) approach is useful for analyzing the composition and origin of the calculated states. Combining these techniques, the specific states making major contributions to the SHG response were identified (Figures 6 a,b). Both stackings exhibit almost identical band-resolved results, their integral contribution, and DOS. In the *AA* stacking, the upper region of the valence band (VB) primarily comprises nonbonding 2p orbitals of oxygen, whereas the bottom part of the conduction band (CB) is mainly occupied by hybridized orbitals of boron and oxygen. Generally, optical properties are mainly determined by electronic transitions close to the Fermi energy. The band-resolved integral curve steeply rises within a tiny range from 0 to -1.55 eV, the region that contributes 80% of the VB to the SHG effect, indicating that the frontier orbitals of the VB make a major contribution to the effect. In this region, the nonbonding 2p electronic orbitals of oxygen account for 95% of the total density and, consequently, for 76% of the SHG effect. The integral curve rises relatively slowly in the CB, and the contributions to the SHG effect reach only 42% within a wider region from 7.53 to 10.86 eV, leading to a slower increase in the SHG.

To further identify the spatial distribution of the electronic states dominating the SHG response, the SHG-density method was used. The SHG density can be divided into occupied and unoccupied states of a virtual hole (VH) and virtual electron (VE), respectively. In this work, the VE process was analyzed because it dominates the SHG in the

crystals studied. The $[BO_3]$ and $[B_3O_6]$ units that form delocalized π-type bonds perpendicular to the plane, referred to as favorable structural units with large nonlinear susceptibilities, together with their parallel alignment are thought to produce high nonlinear bulk susceptibilities. The results show that nonbonding 2p electrons of oxygen are the dominant contributor to the SHG coefficient in occupied states (Figure 6c–f). In unoccupied states, the shape of the SHG density around the B and O atoms reveals a clear contribution from the π and π^* states of the B−O bonds.

The analysis above shows that the *AA* and *AB* stackings have similar electronic structures and an identical NLO mechanism. To further explore the reason for a larger band gap and stronger NLO susceptibility of the *AB* stacking, the band gap and d_{22} coefficient were plotted against the layer distance (Figure 7). In the range from 0 to 50 Å, at a large enough distance, the band gaps of both stackings converge to a constant, as do the d_{22} coefficients, because both stackings with large enough layer distances can be regarded as the same 18MR-B_2O_3 monolayer. The band gaps of the 18MR-B_2O_3 monolayer calculated using the HSE06 approximations is 8.06 eV, whereas d_{22} is almost zero because the calculated optical properties are inversely proportional to the cell volume. The EIDs of the *AA* and *AB* stackings are 3.73 and 3.58 Å, and the detailed diagrams in the range from 3 to 4 Å are shown in Figure 7 on the left. In this range, the band gap of the *AB* stacking decreases but remains larger than that of the *AA* stacking at the same distance. At shorter distances, the *AB* stacking has a significantly larger band gap. The values of the SHG coefficient d_{22} were calculated with the scissors operator (Figure 7). In both stackings, d_{22} decreases globally as the interlayer distance grows, though d_{22} increases slowly
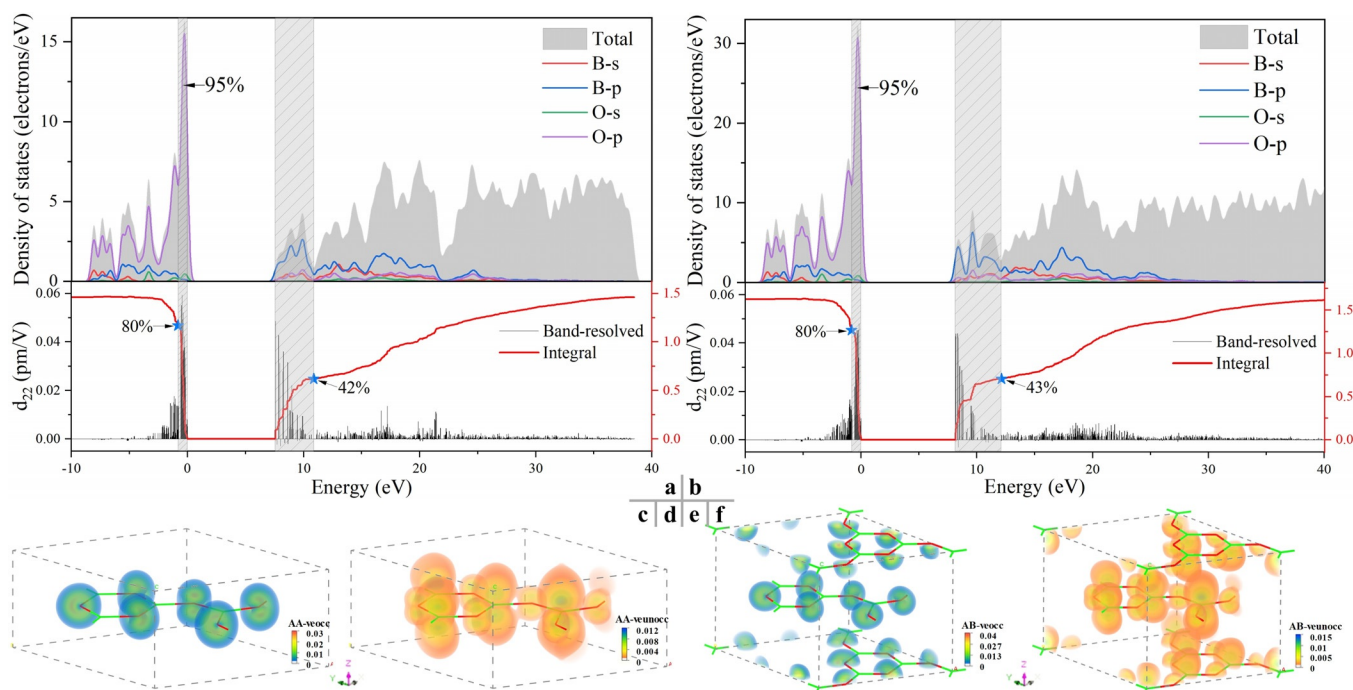
Figure 6. PDOS and band-resolved and integral d_{22} of the a) *AA* and b) *AB* stackings. SHG density of occupied (veocc) and unoccupied (veunocc) states of a virtual electron of the c, d) *AA* and e, f) *AB* stackings.
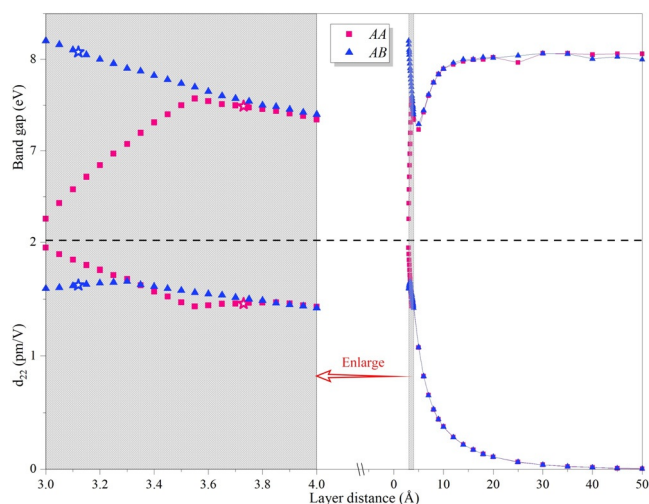
Figure 7. Bandgap and d_{22} vs. layer distance in the *AA* and *AB* stackings. Bandgaps were calculated using the HSE06 approximations; the d_{22} values were calculated with the scissors operation.

around their respective EID range from 3.0 to 3.3 Å for the AB stacking and from 3.55 to 3.85 Å for the AA stacking. Because of shorter EID of the *AB* stacking, d_{22} of *AB* stacking with EID is larger than that of the *AA* stacking. The analysis makes it possible to suggest that the advantages of the band gap and d_{22} for the *AB* stacking mainly originate from its shorter EID. Moreover, the properties of bulk 18MR-B_2O_3 can be tuned by varying the layer stackings, which provides an effective approach for further enhancement.

Conclusion and Outlook

A novel approach for predicting vdW materials was proposed to assist the discovery of NLO materials. Three excellent NLO layers of B_2O_3 with optimal structures and dynamic stability were obtained -12MR-, 18MR-, and 24MR-B_2O_3,—achieving high polymerization of the NLO-active motif [BO_3]. The analysis of the structure counterpart and energy led us to use 18MR-B_2O_3, with 1:1 ratio of [BO_3] and [B_3O_6], to construct a 3D bulk utilizing five stackings: *AA*, *AB*, *AA′*, *AB′*, and *AC′*. Two of them, *AA* and *AB*, exhibit short absorption edges of ≈ 166 and ≈ 154 nm. In addition, they have extremely large SHG coefficients of 1.46 and 1.63 pm/V—more than 3 times larger than that of KBBF, and comparable to that of BBO. The large birefringences at 400 nm of 0.186 and 0.196 for the *AA* and *AB* stackings guarantee that the PM wavelength reaches the short UV edge. The calculated band gap and SHG coefficient d_{22} reveal that the shorter EID allows the *AB* stacking to have a larger band gap, higher NLO susceptibility, and stronger birefringence than those of the *AA* stacking. The results indicate that this vdW materials prediction approach provides a new and effective way for exploring DUV NLO crystals. In future, benefiting from layer feature of vdW materials and DUV transmittance of 18MR-B_2O_3, promising application of 18MR-B_2O_3 series materials will be achieved in the integrated on-chip DUV light sources.

[1] a) A. R. Oganov, C. J. Pickard, Q. Zhu, R. J. Needs, *Nat. Rev. Mater.* **2019**, *4*, 331–348; b) A. R. Oganov, G. Saleh, A. G. Kvashnin, *Computational Materials Discovery*, Royal Society of Chemistry, **2019**; c) S. Atahan-Evrenk, A. Aspuru-Guzik, *Prediction and Calculation of Crystal Structures*, Springer, **2014**; d) A. R. Oganov, *Modern Methods of Crystal Structure Prediction*, John Wiley & Sons, **2011**.

[2] a) A. O. Lyakhov, A. R. Oganov, H. T. Stokes, Q. Zhu, *Comput. Phys. Commun.* **2013**, *184*, 1172–1182; b) A. R. Oganov, C. W. Glass, *J. Chem. Phys. C* **2006**, *124*, 244704; c) Q. Zhu, D. Y. Jung, A. R. Oganov, C. W. Glass, C. Gatti, A. O. Lyakhov, *Nat. Chem.* **2013**, *5*, 61–65; d) X. Dong, A. R. Oganov, A. F. Goncharov, E. Stavrou, S. Lobanov, G. Saleh, G.-R. Qian, Q. Zhu, C. Gatti, V. L. Deringer, R. Dronskowski, X.-F. Zhou, V. B. Prakapenka, Z. Konôpková, I. A. Popov, A. I. Boldyrev, H.-T. Wang, *Nat. Chem.* **2017**, *9*, 440–445; e) X.-F. Zhou, X. Dong, A. R. Oganov, Q. Zhu, Y. Tian, H.-T. Wang, *Phys. Rev. Lett.* **2014**, *112*, 085502; f) W. Zhang, A. R. Oganov, A. F. Goncharov, Q. Zhu, S. E. Boulfelfel, A. O. Lyakhov, E. Stavrou, M. Somayazulu, V. B. Prakapenka, Z. Konôpková, *Science* **2013**, *342*, 1502–1505; g) Z. Wei, W. Zhang, H. Zeng, H. Li, Z. Yang, S. Pan, *Dalton Trans.* **2020**, *49*, 5424–5428.

[3] a) P. Gong, L. Kang, Z. Lin, *J. Am. Chem. Soc.* **2020**, *142*, 15157–15163; b) B. Zhang, X. Zhang, J. Yu, Y. Wang, K. Wu, M.-H. Lee, *Chem. Mater.* **2020**, *32*, 6772–6779; c) J. Zhou, Y. Liu, H. Wu, H. Yu, Z. Lin, Z. Hu, J. Wang, Y. Wu, *Angew. Chem. Int. Ed.* **2020**, *59*, 19006–19010; *Angew. Chem.* **2020**, *132*, 19168–19172; d) Q. Ding, X. Liu, S. Zhao, Y. Wang, Y. Li, L. Li, S. Liu, Z. Lin, M. Hong, J. Luo, *J. Am. Chem. Soc.* **2020**, *142*, 6472–6476; e) H. Wu, B. Zhang, H. Yu, Z. Hu, J. Wang, Y. Wu, P. S. Halasyamani, *Angew. Chem. Int. Ed.* **2020**, *59*, 8922–8926; *Angew. Chem.* **2020**, *132*, 9007–9011; f) X. Lu, Z. Chen, X. Shi, Q. Jing, M.-H. Lee, *Angew. Chem. Int. Ed.* **2020**, *59*, 17648–17656; *Angew. Chem.* **2020**, *132*, 17801–17809; g) C. Wu, G. Yang, M. G. Humphrey, C. Zhang, *Coord. Chem. Rev.* **2018**, *375*, 459–488.

[4] a) T. Schneider, *Nonlinear Optics in Telecommunications*, Springer, Heidelberg, **2004**; b) D. N. Nikogosyan, *Nonlinear Optical Crystals: A Complete Survey*, Springer, Heidelberg, **2006**; c) M. G. Papadopoulos, A. J. Sadlej, J. Leszczynski, *Non-Linear Optical Properties of Matter*, Springer, Heidelberg, **2006**.

[5] M. Mutailipu, S. L. Pan, *Angew. Chem. Int. Ed.* **2020**, *59*, 20302–20317; *Angew. Chem.* **2020**, *132*, 20480–20496.

[6] a) Q. Bian, Z. Yang, Y. Wang, C. Cao, S. Pan, *Sci. Rep.* **2016**, *6*, 34839; b) Q. Bian, Z. Yang, Y. Wang, M. Mutailipu, Y. Ma, S. Pan, *Inorg. Chem.* **2018**, *57*, 5716–5719; c) B. Zhang, E. Tikhonov, C. Xie, Z. Yang, S. Pan, *Angew. Chem. Int. Ed.* **2019**, *58*, 11726–11730; *Angew. Chem.* **2019**, *131*, 11852–11856.

[7] a) F. Liang, L. Kang, P. Gong, Z. Lin, Y. Wu, *Chem. Mater.* **2017**, *29*, 7098–7102; b) L. Kang, Z. Lin, F. Liu, B. Huang, *Inorg. Chem.* **2018**, *57*, 11146–11156; c) L. Kang, F. Liang, Z. Lin, B. Huang, *Sci. China Mater.* **2020**, *63*, 1597–1612; d) L. Kang, F. Liang, X. X. Jiang, Z. S. Lin, C. T. Chen, *Acc. Chem. Res.* **2020**, *53*, 209–217.

[8] X. Chen, Q. Jing, K. M. Ok, *Angew. Chem. Int. Ed.* **2020**, *59*, 20323–20327; *Angew. Chem.* **2020**, *132*, 20503–20507.

[9] a) C. Chen, T. Sasaki, R. Li, Y. Wu, Z. Lin, Y. Mori, Z. Hu, J. Wang, S. Uda, M. Yoshimura, Y. Kaneda, *Nonlinear Optical Borate Crystals: Principals and Applications*, Wiley, Hoboken, **2012**; b) Y. Wang, S. Pan, *Coord. Chem. Rev.* **2016**, *323*, 15–35; c) G. P. Han, Y. Wang, B. B. Zhang, S. L. Pan, *Chem. Eur. J.* **2018**, *24*, 17638–17650.

[10] B. B. Zhang, G. Q. Shi, Z. H. Yang, F. F. Zhang, S. L. Pan, *Angew. Chem. Int. Ed.* **2017**, *56*, 3916–3919; *Angew. Chem.* **2017**, *129*, 3974–3977.

[11] a) C. T. Chen, G. L. Wang, X. Y. Wang, Z. Y. Xu, *Appl. Phys. B* **2009**, *97*, 9–25; b) C. Chen, Y. Wang, B. Wu, K. Wu, W. Zeng, L. Yu, *Nature* **1995**, *373*, 322–324; c) T. T. Tran, N. Z. Koocher, J. M. Rondinelli, P. S. Halasyamani, *Angew. Chem. Int. Ed.* **2017**, *56*, 2969–2973; *Angew. Chem.* **2017**, *129*, 3015–3019; d) G. Peng, N. Ye, Z. Lin, L. Kang, S. Pan, M. Zhang, C. Lin, X. Long, M. Luo, Y. Chen, Y.-H. Tang, F. Xu, T. Yan, *Angew. Chem. Int. Ed.* **2018**, *57*, 8968–8972; *Angew. Chem.* **2018**, *130*, 9106–9110.

[12] a) G. Shi, Y. Wang, F. Zhang, B. Zhang, Z. Yang, X. Hou, S. Pan, K. R. Poeppelmeier, *J. Am. Chem. Soc.* **2017**, *139*, 10645–10648; b) X. Wang, Y. Wang, B. Zhang, F. Zhang, Z. Yang, S. Pan, *Angew. Chem. Int. Ed.* **2017**, *56*, 14119–14123; *Angew. Chem.* **2017**, *129*, 14307–14311; c) Y. Wang, B. Zhang, Z. Yang, S. Pan, *Angew. Chem. Int. Ed.* **2018**, *57*, 2150–2154; *Angew. Chem.* **2018**, *130*, 2172–2176; d) Z. Zhang, Y. Wang, B. Zhang, Z. Yang, S. Pan, *Angew. Chem. Int. Ed.* **2018**, *57*, 6577–6581; *Angew. Chem.* **2018**, *130*, 6687–6691.

[13] C. Chen, *Sci. Sin.* **1979**, *22*, 756–776.

[14] a) C.-H. Lee, G.-H. Lee, A. M. van der Zande, W. Chen, Y. Li, M. Han, X. Cui, G. Arefe, C. Nuckolls, T. F. Heinz, J. Guo, J. Hone, P. Kim, *Nat. Nanotechnol.* **2014**, *9*, 676–681; b) D. N. Basov, M. M. Fogler, F. J. García de Abajo, *Science* **2016**, *354*, aag1992; c) W. Ding, J. Zhu, Z. Wang, Y. Gao, D. Xiao, Y. Gu, Z. Zhang, W. Zhu, *Nat. Commun.* **2017**, *8*, 14956; d) M. Bonilla, S. Kolekar, Y. Ma, H. C. Diaz, V. Kalappattil, R. Das, T. Eggers,

H. R. Gutierrez, M.-H. Phan, M. Batzill, *Nat. Nanotechnol.* **2018**, *13*, 289–293; e) K. S. Burch, D. Mandrus, J.-G. Park, *Nature* **2018**, *563*, 47–52; f) Q. Li, M. Yang, C. Gong, R. V. Chopdekar, A. T. N'Diaye, J. Turner, G. Chen, A. Scholl, P. Shafer, E. Arenholz, A. K. Schmid, S. Wang, K. Liu, N. Gao, A. S. Admasu, S.-W. Cheong, C. Hwang, J. Li, F. Wang, X. Zhang, Z. Qiu, *Nano Lett.* **2018**, *18*, 5974–5980; g) L. Kang, X. Liu, Z. Lin, B. Huang, *Phys. Rev. B* **2020**, *102*, 205424.

[15] J. Wang, N. Umezawa, H. Hosono, *Adv. Energy Mater.* **2016**, *6*, 1501190.

[16] a) G. Ferlat, A. P. Seitsonen, M. Lazzeri, F. Mauri, *Nat. Mater.* **2012**, *11*, 925–929; b) H. Hay, Université Pierre et Marie Curie-Paris VI, **2016**.

[17] a) C. T. Prewitt, R. D. Shannon, *Acta Crystallogr. Sect. B* **1968**, *24*, 869–874; b) H. Effenberger, C. L. Lengauer, E. Parthé, *Monatsh. Chem.* **2001**, *132*, 1515–1517.

[18] C. Chen, N. Ye, J. Lin, J. Jiang, W. Zeng, B. Wu, *Adv. Mater.* **1999**, *11*, 1071–1078.

[19] N. Ye, W. Zeng, B. Wu, C. Chen, *Proc. SPIE-Int. Soc. Opt. Eng.* **1998**, *3556*, 21–23.

[20] S. Zhao, P. Gong, S. Luo, S. Liu, L. Li, M. A. Asghar, T. Khan, M. Hong, Z. Lin, J. Luo, *J. Am. Chem. Soc.* **2015**, *137*, 2207–2210.

[21] R. K. Li, P. Chen, *Inorg. Chem.* **2010**, *49*, 1561–1565.

[22] a) J. Krogh-Moe, *J. Non-Cryst. Solids* **1969**, *1*, 269–284; b) S.-J. Hwang, C. Fernandez, J. P. Amoureux, J. Cho, S. W. Martin, M. Pruski, *Solid State Nucl. Magn. Reson.* **1997**, *8*, 109–121; c) G. Ferlat, T. Charpentier, A. P. Seitsonen, A. Takada, M. Lazzeri, L. Cormier, G. Calas, F. Mauri, *Phys. Rev. Lett.* **2008**, *101*, 065504; d) I. Hung, A. P. Howes, B. G. Parkinson, T. Anupõld, A. Samoson, S. P. Brown, P. F. Harrison, D. Holland, R. Dupree, *J. Solid State Chem.* **2009**, *182*, 2402–2408.

[23] M. Daub, H. Hillebrecht, *Eur. J. Inorg. Chem.* **2015**, 4176–4181.

[24] G. Ferlat, M. Hellgren, F.-X. Coudert, H. Hay, F. Mauri, M. Casula, *Phys. Rev. Mater.* **2019**, *3*, 063603.

[25] a) C. T. Chen, B. C. Wu, A. D. Jiang, G. M. You, *Sci. Sin. Ser. B (Engl. Ed.)* **1985**, *28*, 235–243; b) V. G. Dmitriev, G. G. Gurzadyan, D. N. Nikogosyan, *Handbook of Nonlinear Optical Crystals*, 3rd revised ed., Springer, Berlin, **1999**.

[26] Z. Guoqing, X. Jun, C. Xingda, Z. Heyu, W. Siting, X. Ke, D. Peizhen, G. Fuxi, *J. Cryst. Growth* **1998**, *191*, 517–519.

[27] X. Chen, B. Zhang, F. Zhang, Y. Wang, M. Zhang, Z. Yang, K. R. Poeppelmeier, S. Pan, *J. Am. Chem. Soc.* **2018**, *140*, 16311–16319.

[28] M. J. Dodge, *Appl. Opt.* **1984**, *23*, 1980–1985.